A COMPREHENSIVE MODEL OF NUCLEATE BOILING
FROM A SURFACE WITH A POROUS LAYER

張 榮 興
Ron-Hsin Chang

Energy and Resources Laboratories
Industrial Technology Research Institute

ABSTRACT

A comprehensive model of nucleate boiling heat transfer from a surface with a porous layer was proposed. The boiling process was modeled by mechanisms of liquid intake, thin film evaporation, and vapor outflow. Governing equations for the analysis of hydrodynamics, heat-and-mass transfer and saturation propagation of boiling process were formulated. The solution of these equations resulted predications of velocity profiles of liquid and vapor, liquid saturation profiles, temperature profiles of solid skeleton and liquid in the porous structure, and a complete nucleate boiling curve. The predictions were compared with experimental data. Key variables affecting the performance of a porous surface were outlined and discussed.

INTRODUCTION

Heat transfer surface coated with a thin layer of sintered porous film can lead to enormous enhancement in nucleate boiling and have been found a wide variety of industrial applications. In recent years, many experimental results have been accumulated. However, the existing literatures contain very few informations related to models and correlations for predicting the boiling heat transfer from a surface with a porous layer.

Lu and Chang (1987) studied the effects of the thickness of porous layer, particle diameter, porosity, pore size distribution, and the fluid properties on the dryout heat flux by using the methodology of two phase flow through porous media. Their findings indicated that. dryout heat flux increases with decreasing thickness and increasing particle diameter.

Based on a series of experimental observations, Lu and Chang (1987) analyzed the boiling phenomena in a porous structure as a problem of two phase counter-flow with heat and mass transfer in the porous matrix. The vapor flows upward and the liquid flows downward to make up for the evaporated liquid. Heat is transferred from the base wall to the solid skeleton, to the liquid film between the vapor phase and the solid skeleton, and to evaporate the liquid film. When the liquid supply is insufficient, dryout of the matrix occurs (Lu and Chang, 1987).

The purpose of this paper is to extend our previous hydrodynamic analysis (dryout model; Lu and Chang, 1987) and thermodynamic analysis (Chang and Lu, 1986) to a theoretical nucleate boiling model which includes our previous analyses and a heat-and-mass transfer analysis based on thin film evaporation hypothesis. The hydrodynamic consideration and the heat-and-mass transport processes of the boiling phenomena can now be bridged. The effects of particle diameter, porosity, pore size distribution, thickness, and the properties of fluids are included.

ANALYTICAL MODELING

The phenomena of boiling heat transfer in a porous structure was divided into following phases for modeling purpose.

1. **Liquid Intake.** During boiling, fluid flow through a porous structure is driven primarily by capillary forces. Due to the pumping forces generated by the growth-and-detachment cycle of vapor bubbles, liquid, at a bulk temperature of T_B, is sucked into the porous structure through inactive pores.

2. **Thin Film Evaporation.** The introduced liquid is heated and vaporized in the porous structure. The vapor generated in pores has a barometric pressure due to capillary effects. Therefore, it is possible for the vapor phase to spread along interconnected passages. The interior surface of vapor passages may be covered by a thin liquid film (for annular two phase flow through intermittent pores) or has a meniscus between bubbles (for plug flow in intermittent pores or entrapped vapor bubbles in active pores). The dominant heat transfer mechanisms are presumed to be (1) conduction through the solid skeleton, (2) conduction across the thin liquid film separating the vapor bubble from the solid skeleton, and (3) evaporation of the thin liquid film.

3. **Vapor Outflow.** Vapor generated in the porous structure is forced through intermittent pores, and flows out of the porous structure, resulting countercurrent liquid and vapor flows within the porous structure.

Governing equations for the analysis of hydrodynamics, heat and mass transfer and saturation propagation of the boiling process in porous structure were formulated in the following subsections. The surface structure under consideration was a sintered porous layer of spherical metal powders on a flat plate facing upward, as shown in Fig. 1. However, the analytical model developed here was intended not only for the present surface but for most of porous surfaces and for boiling heat transfer in packed beds.

Vapor-Liquid Countercurrent Flows

The analysis of countercurrent flows of vapor and liquid phases was carried out through the methodology of two phase flow in a porous medium. The superficial velocities of liquid denoted by U_w, and of vapor, denoted by U_v, can be related to the gradient of fluid potential by the Ergun's equation (Bird et al., 1960) modified for two phase flows (Chang, 1987):

$$-\frac{d\Phi_w}{dy} = \frac{v_w U_w}{K\,K_{rw}} + \frac{\beta}{K\,K_{rw}}\,|U_w|\,U_w \quad (1)$$

$$-\frac{d\Phi_v}{dy} = \frac{v_v U_v}{K\,K_{rv}} + \frac{\beta}{K\,K_{rv}}\,|U_v|\,U_v \quad (2)$$

where the variable β was defined by

$$\beta = \frac{1.75}{150}\,\frac{1-\varepsilon}{D_p} \quad (3)$$

The fluid potential, Φ, was defined by

$$\Phi = \frac{P}{\rho} + g\,y \quad (4)$$

The permeability, K, was estimated by the following expression:

$$K = \frac{D_p^2}{150}\,\frac{\varepsilon^3}{(1-\varepsilon)^2} \quad (5)$$

The variable K_{rw} and K_{rv} were the relative permeabilities of liquid and vapor phases, respectively. Each varies from a value of 0 (if the phase is immobile) to 1 (if only that phase exists). Experiments indicated that these coefficients are primarily a function of saturation. Empirical expressions were suggested by Corey (1977) for two phase fluid flow in a nonconsolidated homogeneous and isotropic porous medium.

$$K_{rw} = S^{(3+2/\lambda)} \qquad (6)$$

$$K_{rv} = (1-S)^2 (1 - S^{(1+2/\lambda)}) \qquad (7)$$

where the scaled liquid saturation, S, was given by

$$S = \frac{S_w - S_{w0}}{1 - S_{w0} - S_{v0}} \qquad (8)$$

The variable λ is a pore size distribution index. Brooks and Corey found that the pore size distribution index is about 2 for a typical porous medium, $\lambda \rightarrow \infty$ for the case of uniform pore size distribution. Equations (6) and (7) give $K_{rw} = 0$ at $S_w = S_{wo}$ (with S_{wo} denoting the irreducible liquid saturation) and $K_{rv} = 0$ at $S_v = S_{vo}$ (with S_{vo} denoting the residual vapor saturation). This implies that the liquid phase becomes immobile for $S_w < S_{wo}$ (because of viscosity) while the vapor phase becomes immobile for $S_v < S_{vo}$ (because the vapor phase begins to break up into fine bubbles and is entrapped in re-entrant pores). Another simplified equations for the relative permeabilities were given by Sondergeld and Turcotte (1977) as follows:

$$K_{rw} = S_w \qquad (9)$$

$$K_{rv} = 1 - S_w = S_v \qquad (10)$$

Nonetheless, equations (9) and (10) ignored facts that liquid and vapor became immobile at $S_w < S_{w0}$ and $S_v < S_{v0}$, respectively. Therefore, equations (6) and (7) were used in the present study.

Capillary pressure and Liquid Saturation

Due to the interfacial tension forces, a capillary pressure discontinuity exists between vapor and liquid phases. The pressure difference between vapor and liquid phases was defined as the capillary pressure, P_c:

$$P_c = P_v - P_w \qquad (11)$$

The capillary pressure is directly proportional to the surface tension and inversely proportional to the effective meniscus radius of vapor-liquid interface. The effective meniscus radius is a function of liquid saturation and porous matrix characteristics. Leverett had shown that capillary pressure versus saturation data can be correlated in the following dimensionless form

$$\frac{P_c}{\sigma \sqrt{\varepsilon /K}} = F(S) \qquad (12)$$

This expression implies that the effective meniscus radius is proportional to $\sqrt{K/\varepsilon}$ or $[D_p \varepsilon /(1-\varepsilon)]$. Several equations were available for relating the capillary pressure and the liquid saturation. Here, Udell's (1985) correlation of the imbibition capillary pressure data obtained by Leverett for various low porosity media was used.

$$F(S) = a(1 - S) + b(1 - S)^2$$
$$+ c(1 - S)^3 \qquad (13)$$

where $a = 1.417$, $b = -2.120$, and $c = 1.263$.

The subtraction of equation (1) from equation (2) resulted in the following expression for capillary pressure gradient

$$-\frac{dP_c}{dy} = (\frac{\mu_v U_v}{K K_{rv}} - \frac{\mu_w U_w}{K K_{rw}}) - (\rho_w - \rho_v) g$$
$$+ \beta (\frac{\rho_v}{K K_{rv}} |U_v| U_v - \frac{\rho_w}{K K_{rw}} |U_w| U_w) \qquad (14)$$

Through the use of equations (11)-(13), equation (14) can be rewritten in the following form:

$$-\frac{dS}{dy} = [(\frac{\mu_v U_v}{K K_{rv}} - \frac{\mu_w U_w}{K K_{rw}}) + (\frac{\beta\rho_v}{K K_{rv}} |U_v| U_v$$
$$- \frac{\beta\rho_w}{K K_{rw}} |U_w| U_w) \qquad (15)$$
$$- (\rho_w - \rho_v) g] / [\sigma \sqrt{\varepsilon /K} (dF/dS)]$$

Conservation of Mass

Equations of the conservation of mass for liquid and vapor phases, respectively, can be written as

$$\frac{d}{dy}[\rho_w U_w] = -G \qquad (16)$$

$$\frac{d}{dy}[\rho_v U_v] = G \qquad (17)$$

where G is the rate of generation of vapor per unit volume of porous structure.

$$G = \frac{q_p A_b}{h_{fg}} \qquad (18)$$

The variable q_p is the heat flux from particle to liquid, and can be written as

$$q_p = k_w \frac{(T_s - T_{vw})}{\delta} \qquad (19)$$

where δ is the average thickness of liquid film, T_{vw} is the liquid temperature at vapor-liquid interfaces and is given by (Chang and Lu, 1986)

$$T_{vw} = T_{sat} [1 + \frac{1}{\rho_v h_{fg}} \sigma \sqrt{\varepsilon /K} \cdot F(S)] \qquad (20)$$

The variable A_b is the specific surface area of porous structures.

$$A_b = \frac{6(1 - \varepsilon)}{D_p} \qquad (21)$$

Saturation Propagation Equation

Equation (15) can be rearranged to the following form for the calculation of liquid saturation in the porous structure.

$$-\sigma \sqrt{\varepsilon /K} \frac{d}{dy}[(\frac{dF}{dS}) \frac{dS}{dy}] =$$
$$\frac{1}{K K_{rv}}(v_v + 2 |U_v|) \frac{d}{dy}(\rho_v U_v) -$$
$$- \frac{1}{K K_{rw}}(v_w + 2 |U_w|) \frac{d}{dy}(\rho_w U_w) +$$

$$+ (\frac{\mu \ _v U_v}{K} + \frac{\beta \rho \ _v}{K} |U_v| \ U_v) \ \frac{d}{dy} (\frac{1}{K_{rv}}) \ -$$

$$- (\frac{\mu \ _w U_w}{K} + \frac{\beta \rho \ _w}{K} |U_w| \ U_w) \ \frac{d}{dy} (\frac{1}{K_{rw}}) \qquad (22)$$

The use of equations (6), (7), (16) and (17) in above equation resulted the following second order non-linear ordinary differential equation

$$\frac{\sigma \ \sqrt{\epsilon} \ / K}{M} \ \frac{d}{dy} [(\frac{dF}{dS}) \ \frac{dS}{dy}] + W \ \frac{dS}{dy} + \Omega \ = 0 \qquad (23)$$

where

$$M = \epsilon \ [\frac{\mu \ _v + 2\beta \rho \ _v |U_v|}{K \ K_{rv}} + \frac{\mu \ _w + 2\beta \rho \ _w |U_w|}{K \ K_{rw}}] \qquad (24)$$

$$W = [(\frac{\mu \ _v U_v}{K} + \frac{\beta \rho \ _v}{K} |U_v| U_v) \ \frac{d}{dS} (\frac{1}{K_{rv}})$$
$$- (\frac{\mu \ _w U_w}{K} + \frac{\beta \rho \ _w}{K} |U_w| U_w) \ \frac{d}{dS} (\frac{1}{K_{rw}})]/M \qquad (25)$$

$$\Omega \ = [\frac{\nu \ _v + 2\beta |U_v|}{K \ K_{rv}} + \frac{\nu \ _w + 2\beta |U_w|}{K \ K_{rw}}] \ G/M \qquad (26)$$

Equation (23) provided a equation for calculating the spatial distribution of liquid saturation in porous structure.

Thermal Energy Equation

As discussed previously, the dominant heat transfer mechanisms are conduction through the solid skeleton and conduction across the thin liquid film, as shown in Fig.1. Therefore, the energy equation for the solid skeleton can be written as

$$k_{eff} \ \frac{d^2 T_s}{dy^2} - A_b \ q_p = 0 \qquad (27)$$

with the following boundary conditions

$$- k_{eff} \ \frac{dT_s}{dy} = (Q/A) \ ; \ at \ y=0 \ , \ t>0 \qquad (28)$$

$$- k_{eff} \ \frac{dT_s}{dy} = h_c(T_s - T_{sat}) \ ; \ at \ y=L, \ t>0 \qquad (29)$$

where the variable (Q/A) was the wall to particle heat flux at the bottom of porous layer, k_{eff} was the effective thermal conductivity of solid skeleton, and h_c was the convective heat transfer coefficient at the top of porous layer.

If the porous layer was sufficiently thick and the wall heat flux (Q/A) was sufficiently high, liquid subsequent to boiling is likely to leave the bed dry in spite of the overlying liquid pool (Lu and Chang, 1987). Upon dryout the heat transfer mechanism was dominated by conduction and radiation. However, under normal nucleate boiling conditions temperature of solid skeleton was quite low, radiation heat transfer might be neglected in the analysis. Thermal energy equation for the solid skeleton in the dryout zone can be written as

$$k_{eff} \ \frac{d^2 T_s}{dy^2} = 0 \ ; \ for \ S = 0 \qquad (30)$$

Effective Thermal Conductivity

Three basic regular patterns – the simple cubic, body centered cubic, and hexagonal close packing – were used as simplified models to analyze the conduction heat transfer in a porous layer of uniform spheres. Since each layer of a regular packing is isothermal for a given packing pattern, only those points in contact with a layer above or below are of interest to the analysis.

For the case of simple cubic packing, consider a single sphere of radius R between two planes A and B where A was at a higher temperature than B. There was a finite contact spot between the sphere and each of the other spheres at planes A and B, respectively. Heat was transferred by conduction through the sphere between the two planes and by conduction across the thin liquid film between vapor bubbles and solid surfaces. This configuration was shown in Fig. 2a. Since the conduction heat transfer across the thin liquid film has been take into account in the formulation of equation (19), the system can be simplified to Fig. 2b for the purpose of determining the effective thermal conductivity of solid skeleton. Assuming both the heat flux from plane A to the sphere and that leaved the sphere into plane B were equal and had a value of q_c. Intrinsic thermal conductivity of the sphere was a constant value of k_s. The steady state temperature field in the sphere can be described by the Laplace equation

$$\frac{\partial}{\partial r} (r^2 \ \frac{\partial T}{\partial r}) + \frac{1}{Sin\theta} \ \frac{\partial}{\partial \theta} (Sin\theta \ \frac{\partial T}{\partial \theta}) = 0 \qquad (31)$$

with the following boundary conditions

$$k_s \ (\frac{\partial T}{\partial r}) = q_c \ ; \ at \ r=R, \ 0 \le \theta \le \theta_o$$

$$k_s \ (\frac{\partial T}{\partial r}) = 0 \ ; \ at \ r=R, \ \theta_o \le \theta \le \pi-\theta$$

$$k_s \ (\frac{\partial T}{\partial r}) = -q_c \ ; \ at \ r=R, \ -\theta_o \le \theta \le \pi \qquad (32)$$

where $\theta_o = Sin^{-1}(r_c/R)$. The analytical solution of Eq.(31) was

$$T(r,\theta) = \sum_{n=1}^{\infty} \ \frac{R}{n} \ \frac{q_c}{k_s} \ (\frac{r}{R})^n \ [P_{n-1}(Cos\theta_o) \ -P_{n+1}(Cos\theta_o)] \ P_n(Cos\theta) \qquad (33)$$

where $P_n(x)$ is the Legendre polynomials of n-th order.

The effective thermal conductivity of the solid skeleton, k_{eff} can be defined by a energy balance on a cubical volume of side 2R.

$$r_c^2 \ q_c = k_{eff,sc} \ \frac{T(R,0) - T(R,\pi)}{2 R} \ 4R^2 \qquad (34)$$

or

$$\frac{k_{eff,sc}}{k_s} = \frac{\pi \ (r_c \ / R)^2}{4 \sum_{n=1}^{\infty} \frac{P_{2n-2}(Cos\theta_o) - P_{2n}(Cos\theta_o)}{2n - 1}} \qquad (35)$$

In the case of body centered cubic packing there were three contact points on each plain, and there were four contact points on each plain for hexagonal close packing. Therefore, effective thermal conductivities for body centered cubic packing and hexagonal close packing were written, respectively, as (Balakrishnan and Pei, 1978)

$$k_{eff,BCC} = 3 \ k_{eff,sc} \qquad (36)$$
$$k_{eff,HC} = 4 \ k_{eff,sc} \qquad (37)$$

Theoretical prediction of the effect of contact size (r_c/R) and packing modes on the effective thermal conductivity was shown in Fig. 3. From the figure it can be seen that the body-centered and face-centered cubic configurations yielded larger k_{eff} values than the simple cubic case, and a larger contact size gives a larger k_{eff} value. Since the contact size and packing configuration are determined by the

sintering process, the effect of contact size and packing configuration on the effective thermal conductivity was equivalent to the effect of sintering conditions.

Effective liquid film thickness

Whether the interior surface of the vapor passages is covered by a thin liquid film or has a meniscus between bubbles depends on whether a plug or annular two-phase flow regime exists. The effective liquid film thickness and effective meniscus radius were given as

$$\delta = [(1 - S)^{-1/(\xi+1)} - 1] \, r_v \qquad (38)$$

$$r_v = \frac{1}{\sqrt{\varepsilon}/K \; F(S)} \qquad (39)$$

where $\xi = 1$ for cylindrical vapor channels, and $\xi = 2$ for spherical bubbles. Eqs. (38) and (39) were required for the prediction of the heat flux from particles to liquid, by using Eq.(19).

The dependence of liquid film thickness and effective meniscus radius on the liquid saturation and on the parameter ξ were shown in Fig. 4 for a porous layer with $D_p = 100 \, \mu$ m and $\varepsilon = 0.4$. The effect of ξ on the thickness of liquid film was not significant.

Boundary Conditions

The theoretical model was composed of four coupled non-linear differential equations, eqs.(16), (17), (23), and (27), with the following boundary conditions

$$U_v = 0 \qquad \text{at} \quad y = 0 \qquad (40)$$

$$U_v = \frac{(Q/A)}{\rho_v \, h_{fg}} \qquad \text{at} \quad y = L \qquad (41)$$

$$-k_{eff} \frac{d T_s}{dy} = (Q/A) \quad \text{at} \quad y=0 \qquad (42)$$

$$-k_{eff} \frac{d T_s}{dy} = h_c \, (T_s - T_{sat}) \quad \text{at} \; y=L \qquad (43)$$

$$S = S_L \qquad \text{at} \quad y = L \qquad (44)$$

where S_L is the liquid saturation at the upper surface of porous layer. Determination of S_L can be found elsewhere (Lu and Chang, 1987).

NUMERICAL COMPUTATION

Due to the nonlinearity of the differential equation models, it is hardly possible to solve these models analytically. The only practical approach to solve these models is to obtain numerical solutions via digital computer. The procedures of numerical computation for the model were described below.

1. Specify the surface structure characteristics (particle diameter, porosity, pore size distribution, thickness, contact size r_c, and thermal conductivity of particles) and fluid properties.
2. Calculate β and K from equations (3) and (5), respectively.
3. Estimate U_v from $U_v = (Q/A)/\rho_v \, h_{fg}$.
4. Compute $S(y)$ by solving equation (15) or (23).
5. Calculate δ (y) from equation (38).
6. Compute T_s (y) by solving equations (27) and/or (30).
7. Compute U_v (y) by solving equation (17).
8. Repeat procedures (4), (5), (6) and (7), till the convergence is obtained.
8. Calculate the wall superheat $\Delta T = T_s(y=0) - T_{sat}$.

The implicit finite difference scheme with double precision arithmetic were adopted in the computation work.

EXPERIMENT

The experimental equipment can be divided into four parts: the heat transfer surface, the boiling chamber and condenser, the heater

block, and the temperature measurement system. Fig. 5 is the component diagram of the apparatus.

The heat transfer surfaces were made of copper. Spherical bronze powders were sintered on the upper flat circular end of the test specimen. The number of layers of sintered matrix was calculated by its weight. Boiling occurred on the top of the surface while the bottom of the specimen was in direct contact with the heater block.

The heater block was also made of copper. Heat was generated by three cartridge heaters (max. 1.1 kW) and one wire heater embedded in the copper block (max. 1.2 kW).

The chamber was a Pyrex pipe with 6.0 cm in diameter and 18.0 cm in length, which was nested inside another Pyrex pipe. The air temperature between these glass cylinders was controlled to near but slightly less than the saturation temperature of the liquid to be boiled. Vapor was generated in the boiling chamber, raised through an electrically heated glass pipe, and condensed in a condenser. The condensate was then preheated to its saturation temperature and returned to the boiling chamber. Methanol were used as the boiling liquid. The operation pressure was at 101.3 kPa.

Eight thermocouple wells were drilled in the test specimen as shown in Fig. 6. Four of the wells were 2.0 cm deep and the others were 1.0 cm deep. The thermocouples were copper-constantan wires. The thermocouple conduction error was found to be negligible. Each thermocouple was connected to a data acquisition system or connected to a mv-recorder (Yokogawa model 3046). The data acquisition system was basically composed of an analog to digital converter (μ Mac-4000), a personal computer, a RAM card, floppy disk drivers, and a printer. A real time clock was used to adjust the sampling time at convenient values typically from one to several seconds.

The boiling chamber and the test specimen were cleaned by ultrasonic washer and rinsed with acetone before every test. The liquid level was maintained at about 12 to 14 cm above the test specimen. Start-up of a typical experiment run began with deaeration of the working fluid and aging of the test surface by vigorous nucleate boiling at a power level above 200 kW/m² for several hours.

The data were fed to a personal computer for analysis and the output were used to plot the boiling curve of the surface being investigated. This process was continued until the same superheat were obtained when the surface was heated at a specific heat flux. At this time, the test surface was considered to have aged completely and the stable data could be used to plot the boiling curve.

In a steady state run one-dimensional heat conduction was found to exist in the test specimen (Chang, 1981). Therefore, surface heat flux and surface temperature were readily calculated by using the spatial temperature distribution inside the test specimen.

RESULTS AND DISCUSSIONS

Pool boiling heat transfer data were taken for sintered metallic porous surfaces as well as plain surfaces. Steady nucleate boiling curves for methanol are shown in Fig. 7. The dependence of heat flux (Q/A) on the wall superheat ΔT (defined in terms of the temperature difference between the wall and the saturated working fluid) for plain surface (SS-CU-400) is approximately given by $(Q/A) \propto (\Delta T)^5$. The dependence is consistent with the model proposed by Nishikawa et al. (1977).

Visual observations found that the active nucleation site density of porous surface was much higher than that of plain surface at low heat fluxes in the nucleate boiling region. On plain surfaces, the active nucleation site density increases gradually with an increase in heat flux; while it kept nearly constant on porous surfaces. Since the boiling heat transfer is mainly dominated by the vaporization at the liquid-vapor interfaces and the turbulence induced by bubble generation and detachment, the enhancement in heat transfer, as shown in Fig. 7, is large at low heat fluxes and small at high heat fluxes. When the heat flux is lower than 100 kW/m², the porous surfaces exhibited a very clear effect of sintered layer, with nucleate boiling heat transfer improving

significantly as the porous layer is formed on the heating surface. If the heat transfer coefficients are evaluated at constant heat flux, the improvement are about two- to sevenfold over the plain surfaces. When the heat flux is higher than 100 kW/m^2, surfaces with thin porous layer ($L/D_p < 5$) are still very efficient. However, the boiling curve of a surface with a thick porous layer (see Fig. 7) showed a clear reduction in the slope indicating rapid increase in wall superheat relative to the heat flux. This phenomenon is presumed due to the insufficient supply of liquid through the matrix and the onset of dryout in the porous layer. The slope of nucleate boiling curve is usually greater than 1.0 before the onset of dryout. After the onset of dryout, a vapor blanketed layer are formed near the bottom of the porous structure; the dominant heat transfer mechanism is changed form thin film evaporation to heat conduction in the vapor layer, the wall superheat could be written as

$$\Delta T = \frac{(Q/A) \; L_{dry}}{k_{eff}} + (\Delta T)_{boiling} \qquad (45)$$

where the first term is the temperature drop due to heat conduction across the vapor blanketed layer, and the second term due to boiling heat transfer in the liquid saturated layer. The second term is generally smaller than the first one when the thickness of dryout zone L_{dry} is large. Since the thickness of vapor blanketed layer, L_{dry}, increases with increasing heat flux, the slope of boiling curve, according to Eq.(45), is always less than 1.0 after the formation of a vapor blanketed layer. Therefore, a clear reduction in the slope of boiling curve can be observed and it is a good indication of the onset of dryout in the porous layer. The heat flux at which the clear reduction in slope occurred is defined as the dryout heat flux (Lu and Chang, 1987; Chang, 1987).

The predicted boiling curve for methanol on the porous surface CPS-13-07-X was compared to experimental results in Fig. 8. The theoretical predictions agreed very well with the experimental data within the whole nucleate boiling region. The predicted dryout heat flux also agreed fairly well with the experimental result. However, the reduction in the slope of experimental boiling curve was not so sharp as predicted by the model. This was presumed due to the existence of non-homogeneity in the porous structure. In the theoretical analysis, porous layer was assumed to be a homogeneous medium, permeability was computed by using an average particle diameter and a representative porosity, and the pore size distribution index was chosen equal to a typical value of 2 (it should be noted that the value may vary from 0 to ∞). Since the arrangement and contact size of particles might be altered during sintering process, rearrangement of particles and growth of contact spot during sintering may cause the sintered layer to be of non-homogeneity even though the porous layer was made homogeneous originally. The non-homogeneity of the sintered layer can result a non-uniformity of saturation distribution in the porous structure. It was possible only part of the porous matrix dried-out when the dryout heat flux was reached. The measured wall superheat was an average value over the whole surface and was, therefore, slightly higher than the predicted value. Nonetheless, it was worthy to mention that no empirical constant was required in the theoretical model. The agreement between the predicted and experimental results were encouraging.

Theoretical prediction of the effects of thermal conductivity and porosity on the boiling performance of porous surfaces were shown in Fig. 9. The model predicted that the matrix porosity has a significant effect on the boiling performance. The superheat increased with increasing porosity in the low heat flux region (below dryout heat flux), whereas it decreased with increasing porosity in the high heat flux region (above dryout heat flux). From the figure it can also be seen that a surface with a higher effective thermal conductivity had a better heat transfer performance.

Based on the examination of computed results, it was found that dryout heat flux was relatively insensitive to the effective thermal conductivity of porous layer (It should be noted that the effective thermal conductivity of a porous matrix was much lower than the intrinsic value of metal-particles). This conclusion can also be made by a close examination of Fig. 9. Nonetheless, the effect of k_{eff} on the wall superheat at dryout was pronounced, as shown in the figure. Therefore, the theoretical predictions of dryout heat flux for a bottom-heated bed with infinite contact resistance based on hydrodynamic consideration

(such as Lu and Chang (1987)) are also applicable to the case of sintered porous surface. However, for the purpose of predicting wall superheat at dryout, the model developed in this study should be used.

Fig. 10 shows the liquid saturation distribution in a porous matrix at various heat fluxes. A local minimum in the saturation distribution can be found near the bottom of the porous layer. The liquid saturation was decreased as the heat flux was increased. Once dryout was initiated at the bottom of the porous layer, the thickness of two phase zone decreased as the heat flux was increased. The effect of k_{eff} was also shown in this figure. It can be seen that the liquid saturation distribution was not affected significantly by k_{eff}

Fig. 11 showed the vapor velocity distribution in a porous layer at various heat fluxes. The vapor was speeded up in a short distance. It was caused by a rigorous vaporization of liquid at highest temperature portion in the porous structure. Once dryout was initiated, a stagnant vapor-filled zone was formed at the bottom of the porous layer, as shown in the figure. Again, the rigorous vaporization zone was near the interface between dryout and wetted zones.

The distribution of wall superheat in porous layer at various heat fluxes were shown in Fig. 12. The temperature profiles were found to be strongly dependent on the effective thermal conductivity and heat flux. The temperature decreased with increasing distance and leveled off from the rigorous vaporization zone to the top of the surface. When the heat fluxes were lower than dryout heat flux, the whole porous skeleton was maintained at almost the same temperature. However, once the onset of dryout, a large temperature gradient can be found in the dryout zone near the bottom of porous layer.

In closing, it should be noted that the results obtained in this study were based on the relative permeability functions, capillary pressure and average liquid film thickness specified by equations (6, 7), (12, 13) and (38, 39). The uncertainty inherent in these functions were the major source of error in this analysis. However, it was encouraging to have the good agreement between the predicted boiling curve and experimental results as shown in Fig. 8.

CONCLUSIONS

Pool boiling heat transfer on sintered metallic porous surfaces was experimentally investigated. Nucleate boiling curves of methanol on porous surfaces of various thicknesses were obtained. The results showed that both thin porous surfaces and thick porous surfaces can lead to enormous enhancement in nucleate boiling heat transfer in the low heat flux portion. In high heat flux portion, thin porous surfaces were still very efficient, while a clear reduction in the slope of the boiling curve of thick porous surfaces was observed and, therefore, was inefficient in heat transfer. The reduction in the slope was presumed due to insufficient supply of liquid through the porous structure and the onset of dryout near the bottom of the porous layer.

Based on the experimental results a theoretical model of nucleate boiling heat transfer was proposed. The boiling process was divided into three phases: liquid intake, thin film evaporation, and vapor outflow. Governing equations for the analysis of hydrodynamics, heat-and-mass transfer, and saturation propagation in a porous matrix were formulated. Solution procedures were outlined. Theoretical prediction was compared with experimental data. The prediction agreed very well with the experimental data within whole nucleate boiling region.

ACKNOWLEDGMENT

NOTATIONS

A_b : Specific surface area of porous structure, $[m^2/m^3]$
C_p : Heat capacity, $[J/kg-K]$.

D$_p$: Particle diameter, [m].
F(s) : Leverett function, Eqs. (12) and (13), [-].
G : Vapor generation rate per unit volume of porous matrix, [kg/m^3-s].
g : Acceleration due to gravity, [m/s^2].
h$_c$: Convective heat transfer coefficient, [W/m^2-K].
h$_{fg}$: Latent heat of vaporization, [J/kg].
k$_{eff}$: Effective thermal conductivity, [W/m-K].
K$_{rv}$: Relative permeability of vapor phase, [-].
K$_{rw}$: Relative permeability of liquid phase, [-].
k$_s$: Intrinsic thermal conductivity of solid, [W/m-K].
k$_w$: Thermal conductivity of liquid, [W/m-K].
L : Bed thickness, [m].
M : Parameter defined by Eq.(24), [kg/m^3-s].
P : Pressure, [N/m^2].
P : Capillary pressure, [N/m^2].
(Q/A) : Heat flux from bottom wall to porous layer, [W/m^2].
q$_c$: Heat flux at contact spot, [W/m^2].
q$_p$: Heat flux from particle to liquid film, [W/m^2].
R : Radius of particles, [m].
S : Scaled liquid saturation, [-].
S$_v$: Saturation of vapor, [-].
S$_{v0}$: Residual vapor saturation, [-].
S$_w$: Saturation of liquid, [-].
S$_{w0}$: Saturation of liquid in a pendular ring distribution
T$_s$: Temperature of solid skeleton, [K].
T^{sat} : Saturation temperature, [K].
T^{sat} : Temperature at liquid-vapor interface, [K].
U^{vw} : Superficial velocity of vapor phase, [m/s].
U^v : Superficial velocity of liquid phase, [m/s].
W^w : Parameter defined by Eq. (25), [m/s].
y : Position, [m].

GREEK SYMBOLS

β : Parameter defined by Eq. (3), [-].
ε : Porosity, [-].
Φ : Fluid potential defined by Eq. (4), [m^2/s^2].
K : Permeability, [m^2].
λ : Index for pore size distribution, [-].
μ$_v$: Viscosity of vapor, [N-s/m].
μ$_w$: Viscosity of liquid, [N-s/m].
ν$_v$: Kinematic viscosity of vapor, [m^2/s].
ν$_w$: Kinematic viscosity of liquid, [m^2/s].
Ω : Parameter defined by Eq. (26), [1/s].
ρ$_v$: Density of vapor, [kg/m^3].
ρ$_w$: Density of liquid, [kg/m^3].
σ : Surface tension, [N/m].
ξ : Parameter defined in Eq. (38).

SUBSCRIPT

BCC : Body centered cubic packing
dry : Dryout
HC : Hexagonal close packing
sat : Saturation condition
SC : Simple cubic packing
v : Vapor
w : Liquid

REFERENCES

Balakrishnan, A. R., and D. C. T. Pei, (1978) "HEAT TRANSFER IN GAS-SOLID PACKED BED SYSTEM. 2. THE CONDUCTION MODE"; Ind. Eng. Chem. Process Des. Dev., 18 (1), pp.40-46.

Bau, H. H., and K. E. Torrance, (1982) "BOILING IN LOW PERMEABILITY POROUS MATERIAL"; Int. J. Heat Mass Transfer, 25 (1), pp.45-55.

Bird, R. B., W. E. Stewart, and E. N. Lightfoot, (1959) "TRANSPORT PHENOMENA"; 7th printing, Wiley, New York.

Chang, R. H., (1981) "A STUDY ON BOILING SURFACE AND NUCLEATE BOILING"; M.S. thesis, Department of Chem. Eng.,

National Taiwan University, Taipei, Taiwan, R. O. C.

Chang, R. H., (1987) "BOILING FROM A SURFACE WITH A POROUS LAYER"; Ph. D. Dissertation, Department of Chem. Eng., National Taiwan University, Taipei, Taiwan, R. O. C.

Corey, A. T., (1977) "MECHANICS OF HETEROGENEOUS FLUIDS IN POROUS MEDIA"; Water Resources Publ.

Lu, S. M., and R. H. Chang, (1986) "POOL BOILING FROM A SURFACE WITH A POROUS LAYER -- EFFECT OF CAPILLARY PRESSURE ON LIQUID SUPERHEAT"; Proc. Sym. Transport Phenomena and Applications, pp.111-116, Taipei, Taiwan, R. O. C.

Lu, S. M., and R. H. Chang, (1987) "POOL BOILING FROM A SURFACE WITH A POROUS LAYER"; A. I. Ch. E. J., Vol. 33, No. 11, pp. 1813-1828.

Nishikawa, K., and T. Ito, (1983) "AUGMENTATION OF NUCLEATE BOILING HEAT TRANSFER BY PREPARED SURFACES"; Proc. Heat Transfer in Energy Problems, Hemisphere, pp.119-126.

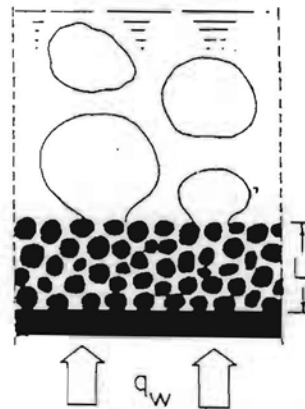Sondergeld, C. H., and D. L. Turcotte, (1977); J. Geophys. Research, vol. 82, pp. 2045-2053.

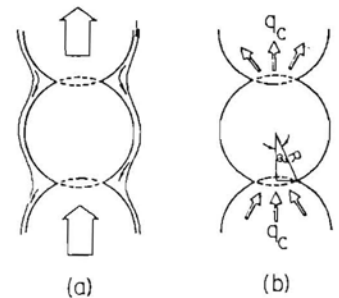Fig. 1 Configuration system for the heat transfer surface with a porous layer.

q$_w$

(a)   (b)

Fig. 2 (a) Thin film evaporation
(b) Simplified conduction model

1 - Body centered cubic
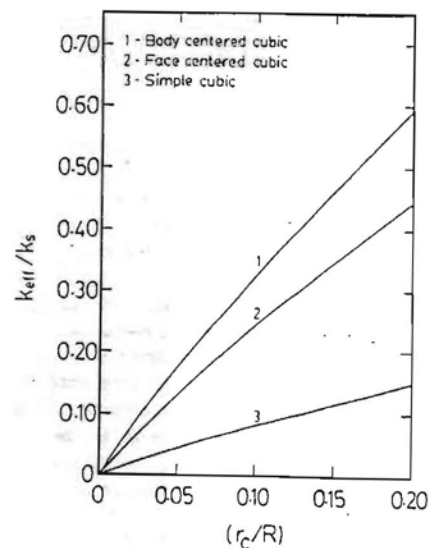2 - Face centered cubic
3 - Simple cubic

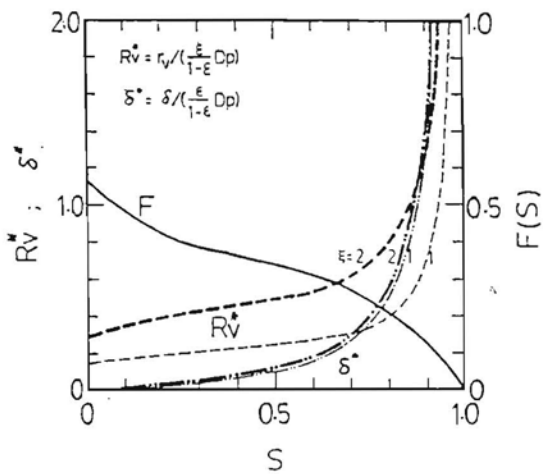Fig. 3 Effect of contact size on the effective thermal conductivity.

Fig. 4　Effects of liquid saturation on Leverett function, bubble radius, and liquid film thickness. $D_p = 100\ \mu$ m, $\varepsilon = 0.4$.
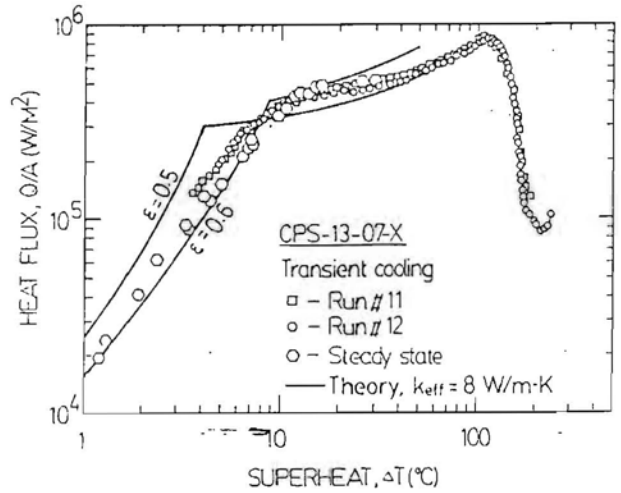
In Fig. 4:
$$R_v^* = r_v/(\tfrac{\varepsilon}{1-\varepsilon}\ D_p)$$
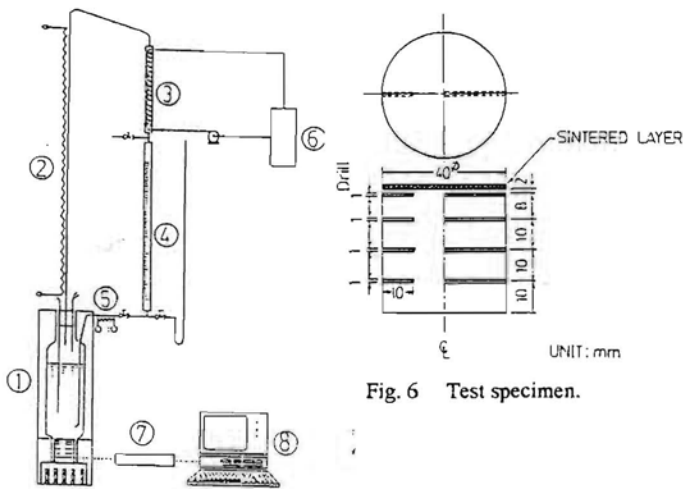$$\delta^* = \delta/(\tfrac{\varepsilon}{1-\varepsilon}\ D_p)$$

Fig. 5　Experiment setup.

(1) Boiler,　　　　(5) Liquid return line,
(2) Vapor raiser,　　(6) Cooling unit,
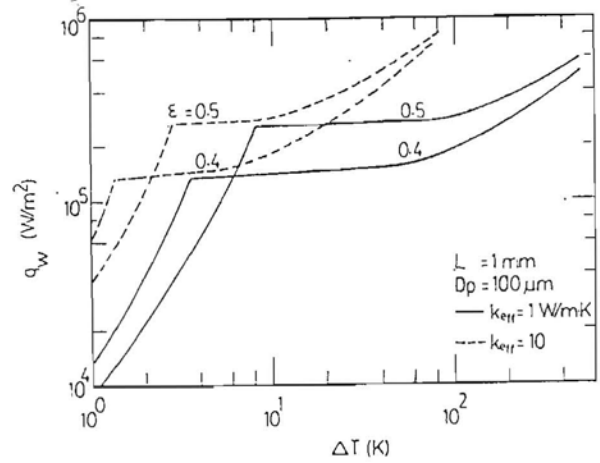(3) Condenser,　　　(7) A/D converter,
(4) Liquid reservoir,　(8) PC computer.

Fig. 6　Test specimen.

Fig. 7　Comparative pool boiling test results for methanol at 101.3 kPa.

Fig. 8　Comparison of the model with experimental data.

Fig. 9　Effects of porosity and effective thermal conductivity on predicted boiling curve. Methanol, 101.3 kPa, Thickness = 1 mm, $D_p = 100\ \mu$ m.

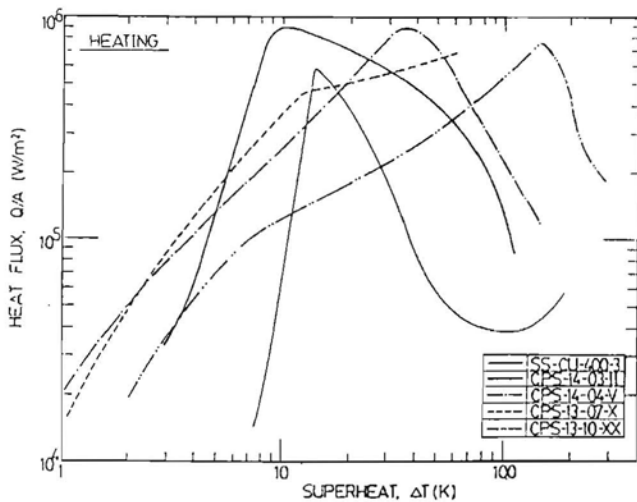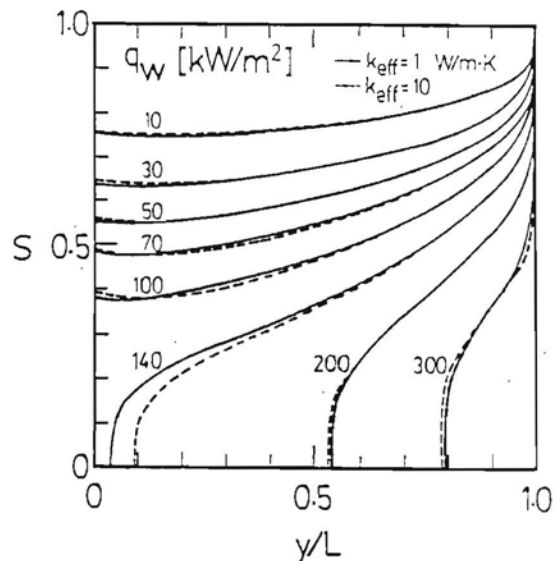Fig. 10　Effects of effective thermal conductivity and wall heat flux on the saturation profile.
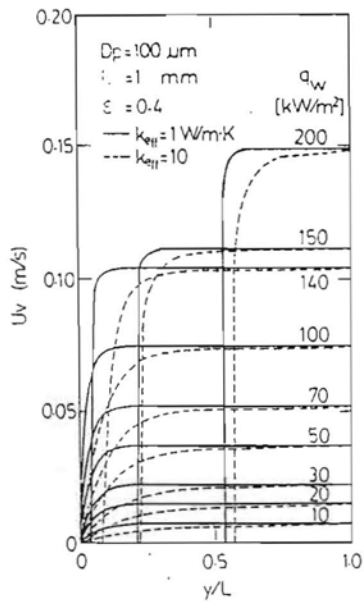
Fig. 11 Effects of effective thermal conductivity and wall heat flux on the velocity profile of vapor flowing in the porous structure.
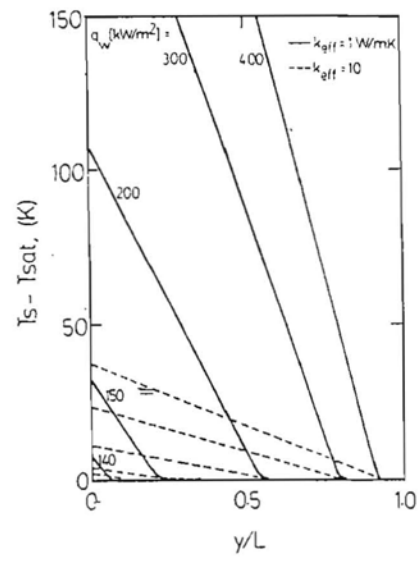

Fig. 12 Effects of effective thermal conductivity and wall heat flux on the temperature profile of the solid skeleton.